Isostructural metal-insulator transition driven by dimensional-crossover in $SrIrO_3$ heterostructures

Shuai Kong,[1,2,3,*] Lei Li,[1,2,3,*] Zengxing Lu,[1,2,3,*] Jiatai Feng,[1,2,3] Xuan Zheng,[1,3,4] Pengbo Song,[5] You-guo Shi,[5] Yumei Wang,[5] Binghui Ge,[6] Katharina Rolfs,[7] Ekaterina Pomjakushina,[7] Thorsten Schmitt,[8] Nicholas C. Plumb,[8] Ming Shi,[8] Zhicheng Zhong,[1,2,3,†] Milan Radovic,[8,9,‡] Zhiming Wang,[1,2,3,§] and Run-Wei Li[1,2,3]

[1]*Key Laboratory of Magnetic Materials and Devices, Ningbo Institute of Materials Technology and Engineering, Chinese Academy of Sciences, Ningbo 315201, China*

[2]*Center of Materials Science and Optoelectronics Engineering, University of Chinese Academy of Sciences, Beijing 100049, China*

[3]*Zhejiang Province Key Laboratory of Magnetic Materials and Application Technology, Ningbo Institute of Materials Technology and Engineering, Chinese Academy of Sciences, Ningbo 315201, China*

[4]*Department of Chemical and Environmental Engineering, The University of Nottingham, Ningbo 315100, China*

[5]*Institute of Physics, Chinese Academy of Sciences, Beijing 100190, China*

[6]*Institutes of Physical Science and Information Technology, Anhui University, Hefei 230601, China*

[7]*Laboratory for Multiscale Materials Experiments, Paul Scherrer Institut, CH-5232 Villigen PSI, Switzerland*

[8]*Swiss Light Source, Paul Scherrer Institut, CH-5232 Villigen PSI, Switzerland*

[9]*SwissFEL, Paul Scherrer Institut, CH-5232 Villigen PSI, Switzerland*

(Received 17 November 2020; revised 26 January 2022; accepted 7 March 2022; published 21 March 2022)

Dimensionality reduction induced metal-insulator transitions in oxide heterostructures are usually coupled with structural and magnetic phase transitions, which complicate the interpretation of the underlying physics. Therefore, achieving isostructural MIT is of great importance for fundamental physics and even more for applications. Here, we report an isostructural metal-insulator transition driven by dimensional-crossover in spin-orbital coupled $SrIrO_3$ films. By using *in situ* pulsed laser deposition and angle-resolved photoemission spectroscopy, we synthesized and investigated the electronic structure of $SrIrO_3$ ultrathin films with atomic-layer precision. Through inserting orthorhombic $CaTiO_3$ buffer layers, combined low-energy electron diffraction measurements and first-principles density functional theory calculations show that the crystal structure of $SrIrO_3$ films remains bulklike with similar oxygen octahedra rotation and tilting when approaching the ultrathin limit. We observe that a dimensional-crossover metal-insulator transition occurs in isostructural $SrIrO_3$ films. Intriguingly, we find the bandwidth of $J_{\text{eff}} = 3/2$ states reduces with lowering the dimensionality and drives the metal-insulator transition. Our results establish a bandwidth controlled metal-insulator transition in the isostructural $SrIrO_3$ thin films.

DOI: 10.1103/PhysRevMaterials.6.034404

I. INTRODUCTION

Oxide heterostructures offer unprecedented opportunities to tune the interactions with similar energy scales, e.g., crystal field splitting, electron correlation and spin-orbit coupling for modulating the ground state of transition metal oxides [1–6]. Among all tuning knobs, dimensionality engineering has emerged as an effective approach to control magnetic and electronic properties in oxides heterostructures in a layer-by-layer manner thanks to the tremendous development of oxide thin film growth [7]. As a prominent example, the metal-insulator transition (MIT) is widely observed in oxide heterostructures through reducing dimensionality [8–15]. However, the dimensional-crossover driven MIT is commonly accompanied by an associated structural phase transition since transition metal oxides exhibit strong coupling between charge, spin, and lattice degrees of freedom [16]. This coexistence obscures the underlying physics, making it difficult to disentangle the different intrinsic interactions that control the MIT. Therefore, achieving an isostructural MIT through dimensional-crossover and consequently controlling physical properties of oxide heterostructures is of great fundamental and technological interest [17,18].

Recently, the 5*d* transition metal iridates emerge as an ideal platform for exploring novel quantum states of matter due to the interplay between strong spin-orbit coupling and electron correlations [5,6,19–21]. Among all iridates, the three-dimensional perovskite $SrIrO_3$ has attracted tremendous attention as a key building block for engineering electronic, magnetic, and topological phases in oxide heterostructure [22–28]. The bulk $SrIrO_3$ exhibits paramagnetic and semimetal behavior with proposed Dirac nodal line and large spin Hall effect, while being at the border of the MIT [28–30]. Through reducing dimensionality, $SrIrO_3$ film undergoes a MIT, accompanied by dramatic changes of the magnetic and structural phases [16,31–33]. Intriguingly, the crystal structure transforms from orthorhombic to tetragonal upon reducing $SrIrO_3$ thickness, where the oxygen octahedra tilting along the [001] direction is suppressed. Such entangled multiple phase transitions have been also reported in the Ruddlesden-Popper series $[(SrIrO_3)_n, SrO]$ [12] and mimic

*These authors contributed equally to this work.
†zhong@nimte.ac.cn
‡milan.radovic@psi.ch
§zhiming.wang@nimte.ac.cn

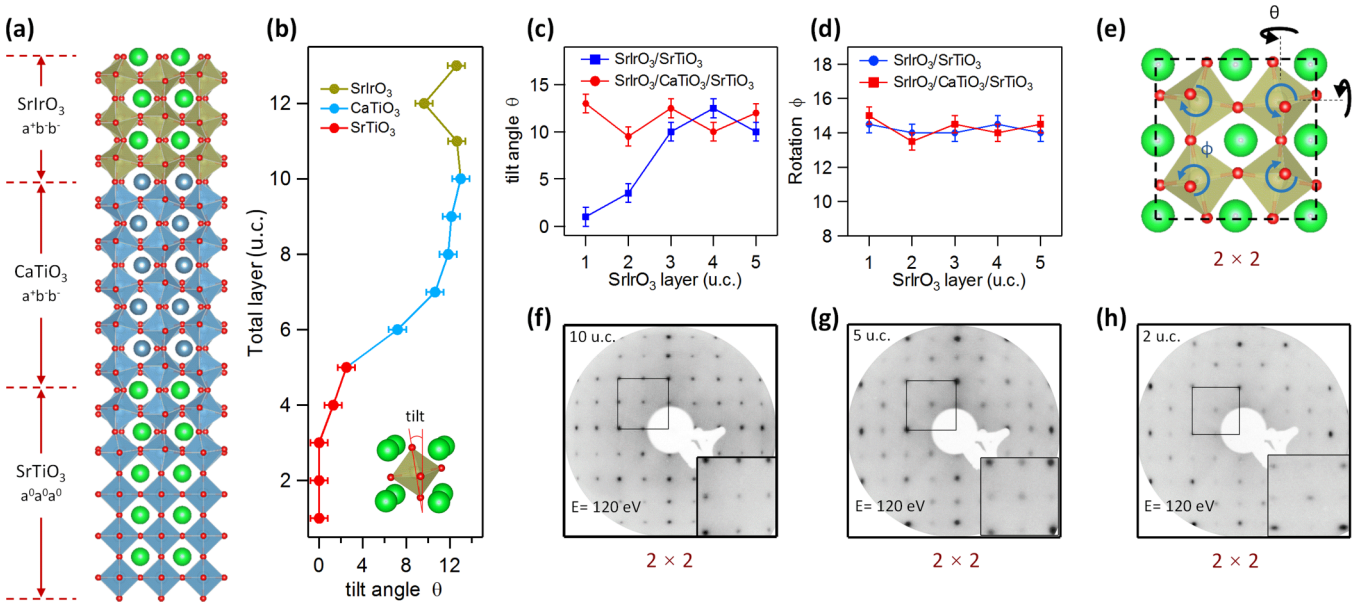

FIG. 1. Control of oxygen octahedral out-of-plane tilting in $SrIrO_3/CaTiO_3$ heterostructures. (a) DFT calculated structure of the $SrIrO_3/CaTiO_3$ heterostructure on Nb:$SrTiO_3$ substrate. (b) DFT calculated layer-dependent tilting angle of the heterostructure. (c) The octahedral out-of-plane tilting and (d) in-plane rotation angles as a function of film thickness with and without $CaTiO_3$ buffer layers. The octahedral tilting is roughly independent on the film thickness after interfacing buffer layers. (d) Top view of structural model. The octahedral out-of-plane tilting and in-plane rotation produce a 2×2 surface periodicity, which has been observed by LEED pattern in 10-, 5-, 2-u.c. $SrIrO_3$ with $CaTiO_3$ buffer layers (f)–(h).

two-dimensional layered [$SrIrO_3$, $SrTiO_3$] superlattices [13], complicating the understanding of the underlying mechanism of the dimensional-crossover driven MIT. Moreover, the structural degree of freedom in iridates plays an important role in the electronic and magnetic properties [34]. To isolate the structural and electronic contribution of the dimensional-crossover driven MIT, it is of great importance to systematically investigate the electronic structure evolution in $SrIrO_3$ ultrathin films, while the structural degree of freedom is kept intact.

In this paper, we demonstrate an isostructural MIT driven by dimensional-crossover in spin-orbital coupled $SrIrO_3$ films. By controlling oxygen octahedral connectivity via inserted orthorhombic $CaTiO_3$ buffer layers, combined low-energy electron diffraction (LEED) measurements and first-principles density functional theory (DFT) calculations show that $SrIrO_3$ ultrathin films in the orthorhombic crystal structure with bulklike oxygen octahedra rotation and tilting during reducing film thickness. Employing *in situ* angle-resolved photoemission spectroscopy (ARPES) we track the evolution of the electronic structure as a function of $SrIrO_3$ film thickness. Intriguingly, we identify that the bandwidth of $J_{\text{eff}} = 3/2$ states shows negligible change in thicker films and starts to decrease when the film thickness is below 4 unit cells (u.c.), leading to an isostructural dimensional-crossover driven MIT in $SrIrO_3$ ultrathin films.

II. RESULTS AND DISCUSSION

Epitaxial $SrIrO_3/CaTiO_3$ heterostructures [see Fig. 1(a)], consisting of varying $SrIrO_3$ thicknesses between 10 and 1 u.c. and fixing $CaTiO_3$ thickness at 5 u.c. as buffer layers, were synthesized by pulsed laser deposition (PLD) on (001) TiO_2-termineted Nb-doped (0.5 wt %) $SrTiO_3$ substrates. The film growth was monitored with atomic u.c. precision by using high-pressure reflection high energy electron diffraction (RHEED). The surface structure of thin films was verified by LEED. After immediately transferring the sample into the ARPES chamber under ultrahigh vacuum condition, *in situ* ARPES measurements were performed at the SIS beamline in Swiss Light Source. First-principles DFT calculations were performed with the generalized gradient approximation using the plane wave VASP package. More details regarding the growth, sample characterization, and DFT calculations can be seen in the Methods section.

Figure 1 summarizes the control of oxygen octahedral out-of-plane tilting in $SrIrO_3$ heterostructures through interface engineering. The orthorhombic $SrIrO_3$ possesses an $a^+b^-b^-$ rotation in Glazer notation [35]. In contrast, the cubic $SrTiO_3$ substrate possesses an $a^0a^0a^0$ rotation without in-plane rotation and out-of-plane tilting at room temperature. Strong mismatch of oxygen octahedra occurs and results in suppression of the out-of-plane tilting in $SrIrO_3$ ultrathin films when grown on the $SrTiO_3$ substrate [16,32,33]. As shown in Ref. [16], the structural transition from orthorhombic to tetragonal during reducing film thickness can be inferred from LEED measurements. This finding is in good agreement with our density functional theory (DFT) calculations shown in Figs. 1(b)–1(d) (details of calculations are described in the Methods section). Intriguingly, after inserting orthorhombic $CaTiO_3$ buffer layers, it is found that both oxygen octahedral out-of-plane tilting and in-plane rotation in $SrIrO_3$ are preserved even in the ultrathin limit. The presence of the out-of-plane tilting and in-plane rotation enlarge surface

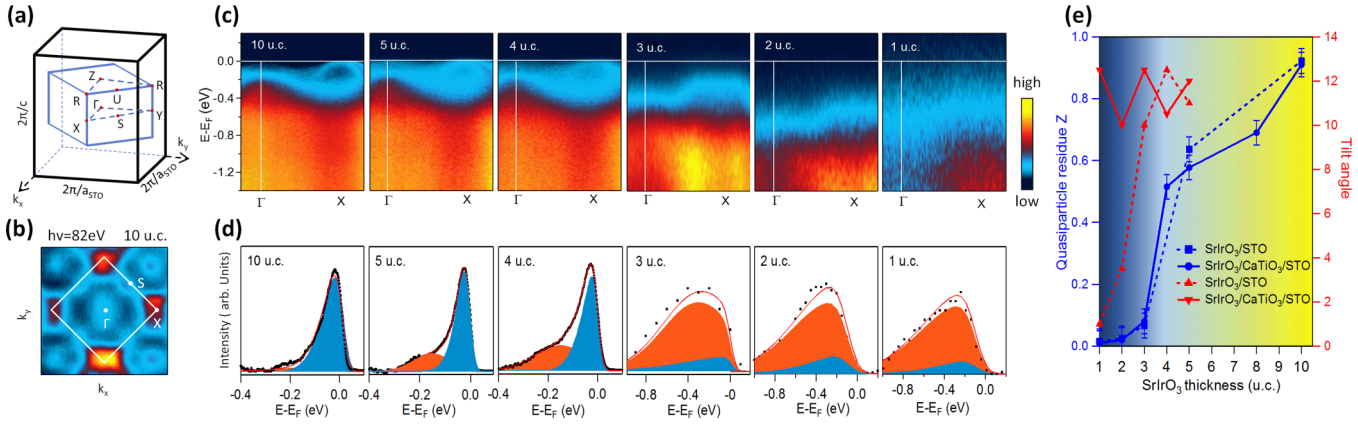

FIG. 2. Dimensional-crossover driven metal-insulator transition in isostructural $SrIrO_3$. (a) The three dimensional Brillouin zone (BZ) of orthorhombic $SrIrO_3$. (b) Fermi surface intensity map measured on 10-u.c. $SrIrO_3/CaTiO_3$ heterostructure. (c) Energy vs momentum intensity maps along Γ-X direction with decreasing $SrIrO_3$ thickness. (d) Energy distribution curves (EDCs) at the Fermi wave vector indicated by the vertical line in the corresponding image plots in (c). An exponential background has been subtracted from the raw EDCs (see Supplemental Material Fig. S2 [36]). (e) The comparison of quasiparticle residue Z and tilting angles for $SrIrO_3$ films grown with and without $CaTiO_3$ buffer layers. All data were taken at a photon energy of 82 eV with circular polarization and at temperature of 14 K.

periodicity as illustrated in Fig. 1(e), giving rise to a 2×2 LEED pattern in Figs. 1(f)–1(h) [16]. Moreover, the 2×2 LEED patterns are present for all the $SrIrO_3/CaTiO_3$ heterostructures with varying $SrIrO_3$ thickness from 10 to 1 u.c. (as seen in Supplemental Material Fig. S1 [36]). Together, our theoretical and experimental results conclusively demonstrate that orthorhombiclike $SrIrO_3$ structure has been stabilized without structural transition during reducing thickness after introducing the $CaTiO_3$ buffer layers.

Previous studies have found concurrent metal-insulator and structural transitions as $SrIrO_3$ film thickness decreases [16,31]. We track how the electronic structure evolves while maintaining the crystal structure intact during reducing $SrIrO_3$ film thickness down to the ultrathin limit. Figure 2(a) gives the three-dimensional Brillouin zone of orthorhombic $SrIrO_3$. Figure 2(b) shows the Fermi surface intensity map of 10-u.c. $SrIrO_3$ grown on a $CaTiO_3$ buffer layer, which displays hole and electron pockets around the Γ, S, and X points, respectively. The Fermi surface is consistent with the semimetal character found in thick $SrIrO_3$ thin films [30,38]. Figure 2(c) show the energy momentum maps along the Γ-X direction of $SrIrO_3/CaTiO_3$ heterostructures with varying $SrIrO_3$ thickness from 10, 5, 4, 3, 2 down to 1 u.c. and $CaTiO_3$ buffer layer fixed at 5 u.c. The band dispersion shows negligible change when the thickness >3 u.c., however, the spectral weight near E_F is gradually suppressed and transferred into higher binding energy during further reducing film thickness, and eventually an energy gap is clearly opened in 2- and 1-u.c. $SrIrO_3$ ultrathin films.

To further characterize the isostructural MIT, we focus now on the evolution of energy distribution curves shown in Fig. 2(d). The coherent quasiparticle peaks around E_F diminish and transfer into incoherent peaks as the film thickness decreases. To describe this quantitatively, we use an effective quasiparticle residue Z by fitting the energy distribution curves (details of the fits are described in Supplemental Material Fig. S2 [36]). The quasiparticle residue Z gradually decreases when the film thickness >3 u.c., below which it suddenly drops nearly to zero. Figure 2(e) shows the comparison of the quasiparticle residue Z and tilting angles as obtained above for $SrIrO_3$ films grown with and without $CaTiO_3$ buffer layers. Similar evolution of Z is observed in $SrIrO_3$ thin films grown on $SrTiO_3$ substrates without $CaTiO_3$ buffer layers (see details in Supplemental Material Fig. S3 [36]), while the evolution of tilting angles differs dramatically. It is clear that the MIT occurs without the structural transition, establishing an isostructural MIT driven by dimensional-crossover in $SrIrO_3$ heterostructures.

In the following, we discuss the mechanism of the dimensional-crossover MIT in isostructural $SrIrO_3$ by taking into account chemical shift and electronic bandwidth (W) of the electronic states. We first show the thickness-dependent evolution of Ir $4f$ core level and O $2p$ valence band to quantify the chemical shift in Fig. 3. Each of the Ir $4f$ spectra exhibits similar spectral features which can be decomposed into two doublets in Fig. 3(a). The doublet feature has been observed previously, corresponding to screened and unscreened components of an Ir^{4+} state [39]. The Ir $4f$ spectra show negligible shifting in binding energy when thickness >3 u.c., while turning to higher binding energy upon further reducing film thickness as marked by black lines in Fig. 3(a). Accordingly, Fig. 3(b) show the spectra of O $2p$ valence band shifting to higher binding energy (see details of O $2p$ valence band with $h\nu = 82$ eV and $h\nu = 70$ eV in Supplemental Material Fig. S4 [36]). The relative chemical shift of Ir $4f$ and O $2p$ are summarized in Fig. 3(c). The cove level and valence band spectra show equivalent shifting of $\sim$0.4 eV to higher binding energy. We note that negligible charge transfer occurs between $SrIrO_3$ and $CaTiO_3$, consistent with recent theoretical calculations [40]. Thus, the observed rigid band shifting cannot induce the dimensional-crossover driven MIT.

Next, we track the evolution of the electronic bandwidth W in the isostructural $SrIrO_3$ heterostructures. Figures 4(a)–4(d) show the photoemission intensity and the corresponding second-derivative maps of 10- and 3-u.c. $SrIrO_3$ with buffer

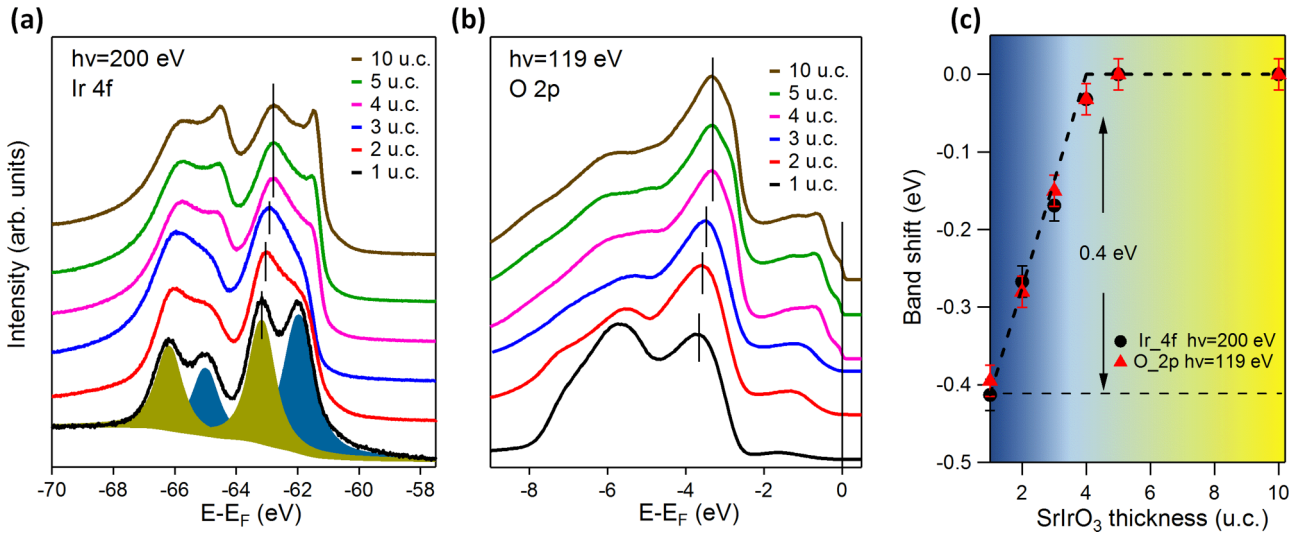

FIG. 3. Thickness-dependent evolution of chemical shift. The spectra of (a) Ir $4f$ core level and (b) O $2p$ valence band as a function of film thickness. The peak positions are marked with black lines. (c) The relative peak shift of both O $2p$ and Ir $4f$ with reference to that of the thick $SrIrO_3$ film.

layers, respectively. The strong dispersive band around the Γ point away from Fermi level of about 0.2 eV is identified as the top position of $J_{\text{eff}} = 3/2$ band as shown in Figs. 4(a)–4(c), which is consistent with theoretical calculations and previous ARPES measurements of bulk $SrIrO_3$ [30,38,41,42]. We note that the $J_{\text{eff}} = 3/2$ band in 3-u.c. thin film shifts significantly to higher binding energy as shown in Figs. 4(b)–4(d). Figure 4(e) shows the systematical evolution of $J_{\text{eff}} = 3/2$ band around Γ point as a function of film thickness (see details in Supplemental Material Fig. S5 [36]). The band dispersions are overlaid on each other and remain almost identical with thickness >3 u.c., while for thinner films they progressively shift to higher binding energy and finally increase to −1.05 eV. The effective mass is extracted by parabolic fits to the holelike bands, which show similar evolution to the film thickness as shown in Supplemental Materials Fig. S6 [36]. This observation agrees with the recent ARPES study of $SrIrO_3$ films grown by oxide molecular beam epitaxy [30]. Meanwhile, we note that the bottom position of $J_{\text{eff}} = 3/2$ band coincides with the onset of the oxygen valence band, consistent with theoretic calculations [43]. The bottom position of $J_{\text{eff}} = 3/2$ states shows a negligible change as the film thickness reduces (see more details in Supplemental Material Fig. S4 [36]). This is in sharp contrast with the band bottom position shift to higher binding energy observed in $SrIrO_3$ films grown directly on $SrTiO_3$ substrates [16], highlighting the important role of oxygen octahedra rotation on the band structure. In Fig. 4(f), we summarize the evolution of $J_{\text{eff}} = 3/2$ band top and bottom position, from which we can determine the $J_{\text{eff}} = 3/2$ states shifting to higher binding energy and the effective bandwidth narrowing by 0.8 eV during reducing the film thickness.

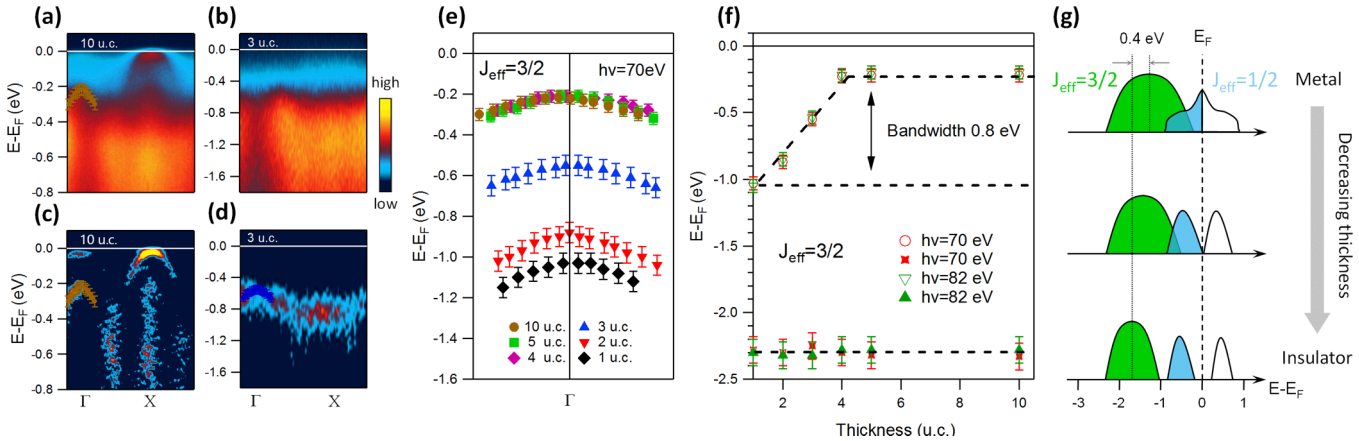

FIG. 4. Mechanism of dimensional-crossover driven metal-insulator transition in isostructural $SrIrO_3$. The photoemission intensity plots of (a) 10-u.c. and (b) 3-u.c. $SrIrO_3$ with $CaTiO_3$ buffer layers taken along Γ-X high symmetry direction. (a),(d) The corresponding second-derivative plots. (e) Evolution of the $J_{\text{eff}} = 3/2$ states around Γ point. The data are extracted from (a)–(d) as a function of film thickness. Details are described in Supplemental Material Fig. S5 [36]. (f) Evolution of band top and bottom position of the $J_{\text{eff}} = 3/2$ states. (g) The thickness-dependent evolution in bandwidth of $J_{\text{eff}} = 3/2$ and $J_{\text{eff}} = 1/2$ states.

In Fig. 4(g), we present the evolution of $J_{\text{eff}} = 3/2$ and $J_{\text{eff}} = 1/2$ states during dimensional-crossover. The observed $J_{\text{eff}} = 3/2$ band narrowing and shifting to higher binding energy features agree well with the optical spectra in Ruddlesden-Popper series [$(SrIrO_3)_n$, SrO] [12,41,44]. The reduction of bandwidth W is understood as breaking of translation symmetry along the z direction, which in turn provides less hopping channels in the ultrathin films. We note that the electron correlation (U) monotonically increases as the dimensionality reduces [16,43]. Moreover, we have also performed first-principles DFT calculations to investigate the structural influence on magnetic states in ultrathin $SrIrO_3$ films. As shown in Supplemental Material Table I [36], the DFT + U + SOC calculations shows that the ultrathin $SrIrO_3$ films favor antiferromagnetic state regardless the crystal structure. This is in consistent with previous calculations [16,31,32]. Therefore, the cooperative effect between the reduction of bandwidth W and enhancement of electron correlation U makes the overall effective bandwidth U/W increase dramatically. The combination of enlarged U/W and formation of antiferromagnetic order in turn triggers the dimensional-crossover driven MIT.

III. CONCLUSION

In conclusion, we demonstrated that the orthorhombiclike $SrIrO_3$ films have been stabilized without a structural transition upon approaching the ultrathin limit through oxygen octahedra rotation engineering by inserting the orthorhombic $CaTiO_3$ buffer layer. Our momentum-resolved band structure measurements revealed that the dimensional-crossover driven MIT occurs in $SrIrO_3$ ultrathin films regardless of the structural transition, which allows us to disentangle the electronic and structural effects in the MIT. We further determined that the reduction of the effective bandwidth plays a crucial role in the dimensional-crossover driven MIT in the isostructural $SrIrO_3$ thin films. Our study provides opportunities for exploring the pure dimensionality effect on the topological phase transitions and spin-orbitronics in isostructural $SrIrO_3$ thin films and heterostructures [28,29].

ACKNOWLEDGMENTS

This work was supported by the National Basic Research of China (Grants No. 2017YFA0303602 and No. 2019YFA0307800), the National Natural Science Foundation of China (Grants No. 12174406, No. U1832102, No. 11874367, No. 51931011, No. 51902322, and No. 11774399), the Key Research Program of Frontier Sciences, Chinese Academy of Sciences (Grant No. ZDBS-LY-SLH008), the Thousand Young Talents Program of China, K. C. Wong Education Foundation (Grant No. GJTD-2020-11), the 3315 Program of Ningbo, the Natural Science Foundation of Zhejiang province of China (Grant No. LR20A040001), the Ningbo Natural Science Foundation (Grants No. 2019A610050 and No. 2019A610055), and the Beijing National Laboratory for Condensed Matter Physics. T.S. was supported by the Swiss National Science Foundation (SNSF) through the Sinergia network Mott Physics Beyond the Heisenberg Model (MPBH) (SNSF Research Grants No. CRSII2_160765/1 and No. CRSII2_141962). M.R. acknowledges support from SNSF via Research Grant No. 200021_182695. The authors acknowledge the beamtime on SIS beamline of the Swiss Light Source and Dreamline of the Shanghai Synchrotron Radiation Facility.

The authors declare that they have no conflict of interest.

APPENDIX: METHODS

1. Sample growth and characterization

Epitaxial $SrIrO_3/CaTiO_3$ heterostructures were synthesized on TiO_2-terminated Nb-doped (0.5 wt %) $SrTiO_3(001)$ substrates by pulsed laser deposition. The heterostructures consist of 5-u.c. $CaTiO_3$ as a fixed buffer layer, and $SrIrO_3$ layers with thickness varying from 1 to 10 u.c. The film growth was monitored with atomic unit cell precision by using high-pressure reflection high energy electron diffraction (RHEED). During growth, the substrate was heated resistively around 750 °C. The oxygen partial pressure during thin film growth was 1×10^{-1} mbar. After growth, the samples were immediately transferred into the analysis chamber under ultrahigh vacuum condition to perform the low energy electron diffraction (LEED) and angle-resolved photoemission spectroscopy (ARPES) measurements. *In situ* ARPES is used to investigate the thickness-dependent evolution of electronic structure of $SrIrO_3$ thin films. ARPES measurements were performed at the SIS beamline in a photon energy range $h\nu = 70$–119 eV. The angular and energy resolutions were better than 0.3 ° and 20 meV, respectively. All samples were measured around 14 K under a vacuum greater than 1×10^{-10} mbar. To overcome the charge-up problem in the insulating samples during the ARPES measurements, conductive Nb-doped $SrTiO_3$ substrates were used. Additionally, a reference spectrum, i.e., Ti $3p$ core level, was used to calibrate the spectra shift. The reference Ti $3p$ core level spectra were measured on the clean Nb-doped $SrTiO_3$ substrates.

2. Density functional theory calculations

Our density functional theory calculations were performed with the Vienna *ab initio* simulation package (VASP) [45,46]. The generalized gradient approximation (GGA) is used to treat the exchange-correlation potential [47]. For structural optimization, we use the k meshes of $4 \times 4 \times 1$ and the cutoff energy for the plane wave of 400 eV for all calculations. We fixed the bottom three layers of atoms of the substrate and a conjugate-gradient algorithm is used to relax the other ions. The convergence criterion is set to 0.001 eV between two ionic steps relaxation. For magnetic ground state calculations in monolayer $SrIrO_3$, the plane-wave cutoff energy is 500 eV and the Brillouin zone integrations are performed with a $5 \times 5 \times 1$ mesh. The in-plane lattice constants are fixed to be the theoretical $SrTiO_3$ lattice. In the magnetic calculations, the spin-orbit coupling and the effective on-site Coulomb interaction of $U_{\text{eff}} = 3.0$ eV are included.

[1] M. Imada, A. Fujimori, and Y. Tokura, Metal-insulator transitions, Rev. Mod. Phys. **70**, 1039 (1998).

[2] P. Zubko, S. Gariglio, M. Gabay, P. Ghosez, and J.-M. Triscone, Interface physics in complex oxide heterostructures, Annu. Rev. Condens. Matter Phys. **2**, 141 (2011).

[3] H. Y. Hwang, Y. Iwasa, M. Kawasaki, B. Keimer, N. Nagaosa, and Y. Tokura, Emergent phenomena at oxide interfaces, Nat. Mater. **11**, 103 (2012).

[4] J. M. Rondinelli, S. J. May, and J. W. Freeland, Control of octahedral connectivity in perovskite oxide heterostructures: An emerging route to multifunctional materials discovery, MRS Bull. **37**, 261 (2012).

[5] W. Witczak-Krempa, G. Chen, Y. B. Kim, and L. Balents, Correlated quantum phenomena in the strong spin-orbit regime, Annu. Rev. Conden. Matter Phys. **5**, 57 (2014).

[6] L. Hao, D. Meyers, M. Dean, and J. Liu, Novel spin-orbit coupling driven emergent states in iridate-based heterostructures, J. Phys. Chem. Solids **128**, 39 (2019).

[7] R. Ramesh and D. G. Schlom, Creating emergent phenomena in oxide superlattices, Nat. Rev. Mater. **4**, 257 (2019).

[8] K. Yoshimatsu, T. Okabe, H. Kumigashira, S. Okamoto, S. Aizaki, A. Fujimori, and M. Oshima, Dimensional-Crossover-Driven Metal-Insulator Transition in $SrVO_3$ Ultrathin Films, Phys. Rev. Lett. **104**, 147601 (2010).

[9] P. D. C. King, H. Wei, Y. Nie, M. Uchida, C. Adamo, S. Zhu, X. He, I. Bozovic, D. G. Schlom, and K. M. Shen, Atomic-scale control of competing electronic phases in ultrathin $LaNiO_3$, Nat. Nanotechnol. **9**, 443 (2014).

[10] D. Toyota, I. Ohkubo, H. Kumigashira, M. Oshima, T. Ohnishi, M. Lippmaa, M. Takizawa, A. Fujimori, K. Ono, M. Kawasaki, and H. Koinuma, Thickness-dependent electronic structure of ultrathin $SrRuO_3$ films studied by in situ photoemission spectroscopy, Appl. Phys. Lett. **87**, 162508 (2005).

[11] A. V. Boris, Y. Matiks, E. Benckiser, A. Frano, P. Popovich, V. Hinkov, P. Wochner, M. Castro-Colin, E. Detemple, V. K. Malik, C. Bernhard, T. Prokscha, A. Suter, Z. Salman, E. Morenzoni, G. Cristiani, H.-U. Habermeier, and B. Keimer, Dimensionality control of electronic phase transitions in nickel-oxide superlattices, Science **332**, 937 (2011).

[12] S. J. Moon, H. Jin, K. W. Kim, W. S. Choi, Y. S. Lee, J. Yu, G. Cao, A. Sumi, H. Funakubo, C. Bernhard, and T. W. Noh, Dimensionality-Controlled Insulator-Metal Transition And Correlated Metallic State in 5d Transition Metal Oxides $Sr_{n+1}Ir_nO_{3n+1}$ ($n = 1$, 2, and ∞), Phys. Rev. Lett. **101**, 226402 (2008).

[13] J. Matsuno, K. Ihara, S. Yamamura, H. Wadati, K. Ishii, V. V. Shankar, H.-Y. Kee, and H. Takagi, Engineering a Spin-Orbital Magnetic Insulator by Tailoring Superlattices, Phys. Rev. Lett. **114**, 247209 (2015).

[14] D. E. McNally, X. Lu, J. Pelliciari, S. Beck, M. Dantz, M. Naamneh, T. Shang, M. Medarde, C. W. Schneider, V. N. Strocov, E. V. Pomjakushina, C. Ederer, M. Radovic, and T. Schmitt, Electronic localization in $CaVO_3$ films via bandwidth control, npj Quantum Mater. **4**, 6 (2019).

[15] Z. Zhong, M. Wallerberger, J. Tomczak, C. Taranto, N. Parragh, A. Toschi, G. Sangiovanni, and K. Held, Electronics with Correlated Oxides: $SrVO_3/SrTiO_3$ as a Mott Transistor, Phys. Rev. Lett. **114**, 246401 (2015).

[16] P. P. Schütz, D. Di Sante, L. Dudy, J. Gabel, M. Stübinger, M. Kamp, Y. Huang, M. Capone, M.-A. Husanu, V. N. Strocov, G. Sangiovanni, M. Sing, and R. Claessen, Dimensionality-Driven Metal-Insulator Transition in Spin-Orbit-Coupled $SrIrO_3$, Phys. Rev. Lett. **119**, 256404 (2017).

[17] R. G. Moore, J. Zhang, V. B. Nascimento, R. Jin, Ji. Guo, G. T. Wang, Z. Fang, D. Mandrus, and E. W. Plummer, A surface-tailored, purely electronic, Mott metal-to-insulator transition, Science **318**, 615 (2007).

[18] D. Lee, B. Chung, Y. Shi, G.-Y. Kim, N. Campbell, F. Xue, K. Song, S.-Y. Choi, J. P. Podkaminer, T. H. Kim, P. J. Ryan, J.-W. Kim, T. R. Paudel, J.-H. Kang, J. W. Spinuzzi, D. A. Tenne, E. Y. Tsymbal, M. S. Rzchowski, L. Q. Chen, J. Lee, and C. B. Eom, Isostructural metal-insulator transition in VO_2, Science **362**, 1037 (2018).

[19] B. J. Kim, Hosub Jin, S. J. Moon, J.-Y. Kim, B.-G. Park, C. S. Leem, Jaejun Yu, T. W. Noh, C. Kim, S.-J. Oh, J.-H. Park, V. Durairaj, G. Cao, and E. Rotenberg, Novel $J_{\rm eff} = 1/2$ Mott State Induced by Relativistic Spin-Orbit Coupling in Sr_2IrO_4, Phys. Rev. Lett. **101**, 076402 (2008).

[20] B. Kim, H. Ohsumi, T. Komesu, S. Sakai, T. Morita, H. Takagi, and T.-H. Arima, Phase-sensitive observation of a spin-orbital Mott state in Sr_2IrO_4, Science **323**, 1329 (2009).

[21] G. Cao and P. Schlottmann, The challenge of spin-orbit-tuned ground states in iridates: A key issues review, Rep. Prog. Phys. **81**, 042502 (2018).

[22] D. Yi, J. Liu, S.-L. Hsu, L. Zhang, Y. Choi, J.-W. Kim, Z. Chen, J. D. Clarkson, C. R. Serrao, E. Arenholz, P. J. Ryan, H. Xu, R. J. Birgeneau, and R. Ramesh, Atomic-scale control of magnetic anisotropy via novel spin-orbit coupling effect in $La_{2/3}Sr_{1/3}MnO_3/SrIrO_3$ superlattices, Proc. Natl. Acad. Sci. U.S.A. **113**, 6397 (2016).

[23] J. Nichols, X. Gao, S. Lee, T. L. Meyer, J. W. Freeland, V. Lauter, D. Yi, J. Liu, D. Haskel, J. R. Petrie, E.-J. Guo, A. Herklotz, D. Lee, T. Z. Ward, G. Eres, M. R. Fitzsimmons, and H. N. Lee, Emerging magnetism and anomalous Hall effect in iridate-manganite heterostructures, Nat. Commun. **7**, 12721 (2016).

[24] L. Hao, D. Meyers, C. Frederick, G. Fabbris, J. Yang, N. Traynor, L. Horak, D. Kriegner, Y. Choi, J.-W. Kim, D. Haskel, P. J. Ryan, M. P. M. Dean, and J. Liu, Two-Dimensional $J_{\rm eff} = 1/2$ Antiferromagnetic Insulator Unraveled from Interlayer Exchange Coupling in Artificial Perovskite Iridate Superlattices, Phys. Rev. Lett. **119**, 027204 (2017).

[25] J. Matsuno, N. Ogawa, K. Yasuda, F. Kagawa, W. Koshibae, N. Nagaosa, Y. Tokura, and M. Kawasaki, Interface-driven topological Hall effect in $SrRuO_3$-$SrIrO_3$ bilayer, Sci. Adv. **2**, e1600304 (2016).

[26] Z. Zeng, J. Feng, X. Zheng, C. Wang, J. Liu, Z. Lu, F.-X. Jiang, X.-H. Xu, Z. Wang, and R.-W. Li, Emergent ferromagnetism with tunable perpendicular magnetic anisotropy in short-periodic $SrIrO_3/SrRuO_3$ superlattices, Appl. Phys. Lett. **116**, 142401 (2020).

[27] D. Xiao, W. Zhu, Y. Ran, N. Nagaosa, and S. Okamoto, Interface engineering of quantum Hall effects in digital transition metal oxide heterostructures, Nat. Commun. **2**, 1 (2011).

[28] Y. Chen, Y.-M. Lu, and H.-Y. Kee, Topological crystalline metal in orthorhombic perovskite iridates, Nat. Commun. **6**, 6593 (2015).

[29] T. Nan, T. J. Anderson, J. Gibbons, K. Hwang, N. Campbell, H. Zhou, Y. Q. Dong, G. Y. Kim, D. F. Shao, T. R. Paudel, N. Reynolds, X. J. Wang, N. X. Sun, E. Y. Tsymbal, S. Y. Choi,

M. S. Rzchowski, Y. B. Kim, D. C. Ralph, and C. B. Eom, Anisotropic spin-orbit torque generation in epitaxial $SrIrO_3$ by symmetry design, Proc. Natl. Acad. Sci. U.S.A. **116**, 16186 (2019).

[30] Y. F. Nie, P. D. C. King, C. H. Kim, M. Uchida, H. I. Wei, B. D. Faeth, J. P. Ruf, J. P. C. Ruff, L. Xie, X. Pan, C. J. Fennie, D. G. Schlom, and K. M. Shen, Interplay of Spin-Orbit Interactions, Dimensionality, and Octahedral Rotations in Semimetallic $SrIrO_3$, Phys. Rev. Lett. **114**, 016401 (2015).

[31] D. J. Groenendijk, C. Autieri, J. Girovsky, M. C. Martinez-Velarte, N. Manca, G. Mattoni, A. M. R. V. L. Monteiro, N. Gauquelin, J. Verbeeck, A. F. Otte, M. Gabay, S. Picozzi, and A. D. Caviglia, Spin-Orbit Semimetal $SrIrO_3$ in the Two-Dimensional Limit, Phys. Rev. Lett. **119**, 256403 (2017).

[32] W. Guo, D. X. Ji, Z. B. Gu, J. Zhou, Y. F. Nie, and X. Q. Pan, Engineering of octahedral rotations and electronic structure in ultrathin $SrIrO_3$ films, Phys. Rev. B **101**, 085101 (2020).

[33] T. C. van Thiel, J. Fowlie, C. Autieri, N. Manca, M. Šiškins, D. Afanasiev, S. Gariglio, and A. D. Caviglia, Coupling lattice instabilities across the interface in ultrathin oxide heterostructures, ACS Mater. Lett. **2**, 389 (2020).

[34] G. Jackeli and G. Khaliullin, Mott Insulators in the Strong Spin-Orbit Coupling Limit: From Heisenberg to a Quantum Compass And Kitaev Models, Phys. Rev. Lett. **102**, 017205 (2009).

[35] A. M. Glazer, Simple ways of determining perovskite structures, Acta Crystallogr. **31**, 756 (1975).

[36] See Supplemental Material at http://link.aps.org/supplemental/10.1103/PhysRevMaterials.6.034404 for details on the growth of ultrathin $SrIrO_3$ films, and thickness-driven metal-insulator transition in $SrIrO_3/CaTiO_3$ and $SrIrO_3/SrTiO_3$ heterostructures, evolution of O 2p valence bands, bandwidth evolution of $J_{eff} = 3/2$ states and evolution of effective mass, which includes Refs. [9,30,32,37,38,40].

[37] Z. Wang, S. M. Walker, A. Tamai, Y. Wang, Z. Ristic, F. Y. Bruno, A. de la Torre, S. Riccò, N. C. Plumb, M. Shi, P. Hlawenka, J. Sánchez-Barriga, A. Varykhalov, T. K. Kim, M. Hoesch, P. D. C. King, W. Meevasana, U. Diebold, J. Mesot, B. Moritz *et al.*, Tailoring the nature and strength of electron–phonon interactions in the $SrTiO_3(001)$ 2D electron liquid, Nat. Mater. **15**, 835 (2016).

[38] Z. T. Liu, M. Y. Li, Q. F. Li, J. S. Liu, W. Li, H. F. Yang, Q. Yao, C. C. Fan, X. G. Wan, Z. Wang, and D. W. Shen, Direct observation of the Dirac nodes lifting in semimetallic perovskite $SrIrO_3$ thin films, Sci. Rep. **6**, 30309 (2016).

[39] L. C. Seitz, C. F. Dickens, K. Nishio, Y. Hikita, J. Montoya, A. Doyle, C. Kirk, A. Vojvodic, H. Y. Hwang, J. K. Norskov, and T. F. Jaramillo, A highly active and stable $IrO_x/SrIrO_3$ catalyst for the oxygen evolution reaction, Science **353**, 1011 (2016).

[40] Z. Zhong and P. Hansmann, Band Alignment and Charge Transfer in Complex Oxide Interfaces, Phys. Rev. X **7**, 011023 (2017).

[41] H. Zhang, K. Haule, and D. Vanderbilt, Effective $J = 1/2$ Insulating State in Ruddlesden-Popper Iridates: An LDA+DMFT Study, Phys. Rev. Lett. **111**, 246402 (2013).

[42] H.-S. Kim, Y. Chen, and H.-Y. Kee, Surface states of perovskite iridates $AIrO_3$: Signatures of a topological crystalline metal with nontrivial Z_2 index, Phys. Rev. B **91**, 235103 (2015).

[43] P. Liu, B. Kim, X.-Q. Chen, D. D. Sarma, G. Kresse, and C. Franchini, Relativistic GW+BSE study of the optical properties of Ruddlesden-Popper iridates, Phys. Rev. Mater. **2**, 075003 (2018).

[44] B. Kim, P. Liu, and C. Franchini, Dimensionality-strain phase diagram of strontium iridates, Phys. Rev. B **95**, 115111 (2017).

[45] G. Kresse and J. Hafner, Ab initio molecular dynamics for open-shell transition metals, Phys. Rev. B **48**, 13115 (1993).

[46] G. Kresse and J. Furthmuller, Efficiency of ab-initio total energy calculations for metals and semiconductors using a plane-wave basis set, Comput. Mater. Sci. **6**, 15 (1996).

[47] J. P. Perdew, K. Bieron, and M. Ernzerhof, Generalized Gradient Approximation Made Simple, Phys. Rev. Lett. **77**, 3865 (1996).